Dynamic Multi-echo DCE- and DSC-MRI in Rectal Cancer: Low Primary Tumor K^{trans} and ΔR_2^* Peak Are Significantly Associated With Lymph Node Metastasis

Endre Grøvik, MSc,[1,2]* Kathrine Røe Redalen, PhD,[3] Tryggve Holck Storås, PhD,[1] Anne Negård, MD, PhD,[4] Stein Harald Holmedal, MD,[4] Anne Hansen Ree, MD, PhD,[3,5] Sebastian Meltzer, MD,[3,5] Atle Bjørnerud, PhD,[1,2] and Kjell-Inge Gjesdal, PhD[4,6]

Purpose: To implement a dynamic contrast-based multi-echo MRI sequence in assessment of rectal cancer and evaluate associations between histopathologic data and the acquired dynamic contrast-enhanced (DCE) and dynamic susceptibility contrast (DSC) -MRI parameters.

Materials and Methods: This pilot study reports results from 17 patients with resectable rectal cancer. Dynamic contrast-based multi-echo MRI (1.5T) was acquired using a three-dimensional multi-shot EPI sequence, yielding both DCE- and DSC-data following a single injection of contrast agent. The Institutional Review Board approved the study and all patients provided written informed consent. Quantitative analysis was performed by pharmacokinetic modeling on DCE data and tracer kinetic modeling on DSC data. Mann-Whitney U-test and receiver operating characteristics curve statistics was used to evaluate associations between histopathologic data and the acquired DCE- and DSC-MRI parameters.

Results: For patients with histologically confirmed nodal metastasis, the primary tumor demonstrated a significantly lower K^{trans} and peak change in R_2^*, R_2^*-$peak_{enh}$, than patients without nodal metastasis, showing a *P*-value of 0.010 and 0.005 for reader 1, and 0.043 and 0.019 for reader 2, respectively.

Conclusion: This study shows the feasibility of acquiring DCE- and DSC-MRI in rectal cancer by dynamic multi-echo MRI. A significant association was found between both K^{trans} and R_2^*-$peak_{enh}$ in the primary tumor and histological nodal status of the surgical specimen, which may improve stratification of patients to intensified multimodal treatment.

Level of Evidence: 4

Technical Efficacy: Stage 2

J. MAGN. RESON. IMAGING 2017;46:194–206

Current international guidelines recommend MRI as part of primary staging of rectal cancer.[1] MRI helps identify patients with increased risk of local recurrence and the need of neoadjuvant chemoradiotherapy (CRT).[2] Despite improvements in multimodal rectal cancer management during the past decades, with local recurrence rates below 10%,[3] a considerable number of patients experience poor disease outcome resulting from metastatic disease progression.[4] Reliable detection of metastatic lymph nodes (N+ stage), a main prognostic indicator of distant metastasis, is still a challenge in rectal cancer MRI. At present, the most accurate criterion is the morphological finding of

View this article online at wileyonlinelibrary.com. DOI: 10.1002/jmri.25566

Received Aug 30, 2016, Accepted for publication Nov 8, 2016.

*Address reprint requests to: E.G., Oslo University Hospital, The Intervention Centre, Sognsvannsveien 20, NO-0027, Oslo, Norway. E-mail: endre.grovik@mn.uio.no

From the [1]Oslo University Hospital, The Intervention Centre, Oslo, Norway; [2]University of Oslo, Department of Physics, Blindern, Oslo, Norway; [3]Akershus University Hospital, Department of Oncology, Lørenskog, Norway; [4]Akershus University Hospital, Department of Radiology, Lørenskog, Norway; [5]University of Oslo, Faculty of Medicine, Blindern, Oslo, Norway; and [6]Sunnmøre MR-klinikk, Ålesund, Norway

irregular-contoured nodes with mixed signal intensities in T_2-weighted MR images. However, these MRI findings are associated with substantial misinterpretation and the diagnostic accuracy is relatively poor. A recent meta-analysis of 21 clinical studies showed a diagnostic accuracy for lymph node staging of 71%.[5]

To improve the ability of MRI to predict patients at risk of developing metastatic disease, considerable interest is focusing on the tumor microenvironment. Dynamic contrast-based MRI is an increasingly popular method for tumor characterization, enabling quantitative assessment of phenotypic properties.[6] The most commonly used dynamic acquisition is dynamic contrast-enhanced (DCE) MRI, enabling assessment of tissue properties such as capillary permeability and extracellular volume fraction.[7] There is currently no consensus concerning the role of DCE-MRI in rectal cancer patients. However, according to a recent study, this technique may improve the detection of nodal metastasis.[8]

Dynamic susceptibility contrast (DSC) MRI is most commonly used to measure perfusion in the brain.[9] However, studies have also shown the feasibility of using this approach to assess microvasculature in rectal cancer[10] and phenotypic characteristics of breast tumors.[11–13] Recognizing that rectal tumors are highly angiogenic, it is hypothesized that DSC-MRI may provide valuable information for assessing pathophysiological properties in this patient group.

Multiple echoes can be acquired in a high temporal resolution dynamic contrast-based MRI sequence, allowing quantitative measurements of the dynamic change in both longitudinal ($R_1 = 1/T_1$) and transverse relaxation rate ($R_2^* = 1/T_2^*$). As a result, DCE- and DSC-data can be obtained during a single dynamic examination, thus yielding information on pathophysiological properties related to both tissue- permeability and perfusion. In earlier studies, the feasibility of a multi-echo MRI technique has been demonstrated through both simulations and in the assessment of breast cancer.[14,15] The use of dynamic multi-echo imaging for combined DCE- and DSC-MRI analysis have also been demonstrated in brain tumors.[16–18]

The aim of this pilot study was to implement a dynamic contrast-based multi-echo MRI sequence in the assessment of rectal cancer, and to evaluate associations between histopathologic data and the attainable DCE- and DSC-MRI parameters.

Materials and Methods

Study Patients

The investigation was performed within a prospective biomarker study approved by the Institutional Review Board and the Regional Committee for Medical and Health Research Ethics. The study was performed in accordance with the Helsinki declaration. Written informed consent was obtained for all patients before participation.

The principal inclusion criterion was histologically confirmed rectal cancer scheduled to radical treatment. The patient cohort within the present study was enrolled between March 2014 and June 2015 and all cases had primary pelvic surgery without neoadjuvant CRT. The study cohort included two patients with a preoperative staging of T4 disease and five patients with a preoperative staging of T3N1 disease. According to national guidelines, one patient did not receive neoadjuvant CRT due to age (above 75 years) and frailty. The other T4 case was not accepted for CRT by the regional radiotherapy center. In six patients with N1 disease, the lymph node had a margin of more than 2 mm from the mesorectal fascia; hence, these were also referred to surgery without neoadjuvant CRT. The resected tumor specimens underwent standard histopathologic staging (pTN), including determination of the absence or presence of extramural venous invasion. Patient and tumor characteristics are provided in Table 1.

MRI Acquisition

In this pilot study, 24 patients were examined, of which five were excluded because of bowel motion and two because of image artifacts. Imaging was performed on a Philips Achieva 1.5 Tesla (T) system (Philips Healthcare, Best, The Netherlands) with NOVA Dual HP gradients (33 mT/m maximum gradient amplitude, 180 T/m/s slew rate). A five-channel cardiac coil with parallel imaging capabilities was applied. To reduce bowel peristalsis, glucagon (1 mg/mL, 1 mL intramuscularly) and Buscopan® (20 mg/mL, 1 mL intravenously) were given immediately before the patient was centered in the scanner. The dose of Buscopan® was divided in two; giving half the dose together with the glucagon and the second half before the dynamic contrast-based MRI acquisition. Conventional high-resolution fast spin-echo T_2-weighted images of the pelvic cavity and rectum were obtained in the sagittal and transversal planes as well as perpendicular to the tumor axis (repetition time (TR) = 2820–3040 ms; echo time (TE) = 80 ms; acquisition matrix = 256 × 230; slice thickness = 2.5 mm; number of averages = 6; and echo train length = 20).

Dynamic contrast-based multi-echo data were acquired by a three-dimensional (3D) T_1-weighted multi-shot EPI sequence with three echoes. TR = 39 ms, TE1 = 4.6 ms, echo spacing = 9.3 ms, flip angle = 28°, EPI factor = 9. The acquired matrix size was 92 × 90 over a 180 × 180 mm field of view. Twelve slices were acquired with a thickness of 10 mm. The temporal resolution was approximately 2 s/imaging volume with 60 dynamic series acquired. A ProSet fat suppression technique was applied along with a parallel imaging (SENSE) factor of 1.7 in the RL direction. All slices were acquired parallel to the T_2-weighted images perpendicular to the tumor axis.

The dynamic multi-echo sequence was interleaved with a high spatial resolution 3D T_1-weighted TFE sequence (THRIVE), as part of a split-dynamic MRI framework detailed in a recent study.[14] In this framework, one set of THRIVE baseline images was initially acquired. The dynamic multi-echo sequence was then started and five to seven baseline acquisitions were obtained before contrast agent (CA) administration. The multi-echo acquisition was repeated approximately 30 times during the wash-in phase, immediately followed by the first postcontrast THRIVE acquisition. During the intermediate and late postcontrast phase, six split sessions were conducted, each containing four multi-echo acquisitions and one THRIVE acquisition. In addition, a series of 14 multi-echo acquisitions were obtained after the last THRIVE

TABLE 1. Patient and Tumor Characteristics*

No. of patients	**17**
Gender	
Male	11 (64.7%)
Female	6 (35.3%)
Median age (years)[a]	66 (50–88)
Male[a]	66 (52–88)
Female[a]	71 (50–77)
Median tumor volume (cm^3)[a,b]	18.8 (4.5–64.0)
rTNM stages[c]	
mrT1	2 (11.8%)
mrT2	5 (29.4%)
mrT3	8 (47.1%)
mrT4	2 (11.8%)
mrN0	10 (58.8%)
mrN1	6 (35.3%)
mrN2	1 (5.9%)
rM0	16 (94.1%)
rM1	1 (5.9%)
Surgery	
Low anterior resection	13 (76.5%)
Abdominal perineal resection	3 (17.6%)
Transanal endoscopic microsurgery	1 (5.9%)
pTN stages[d]	
pT1	4 (23.5%)
pT2	4 (23.5%)
pT3	8 (47.1%)
pT4	1 (5.9%)
pN0	10 (58.8%)
pN1	6 (35.3%)
pN2	1 (5.9%)
Extramural venous invasion[d]	
Yes	6 (35.3%)
No	11 (64.7%)

*Except where indicated, data are numbers of patients, with percentages in parentheses.
[a]Numbers in parentheses are ranges.
[b]Mean tumor volumes calculated from two independent radiologists' tumor delineations in MRI.
[c]Assessed with MRI or CT according to the tumor-node-metastasis system. Prefix 'mr' denotes MRI-assessed staging, prefix 'r' denotes radiologically assessed staging (MR and/or CT)
[d]Determined by histopathological evaluation of the surgical specimens.

acquisition to improve curve fitting for kinetic modeling. To avoid non-steady state effects, dummy repetitions (i.e., no data sampling) were run for 2500 ms at the beginning of each multi-echo segment. Only results from the dynamic multi-echo data are reported in this work.

A dose of 0.2 mL/kg body weight of gadolinium-based CA (Dotarem® 279.3 mg/mL, Guerbet, Roissy, France) was injected as a bolus (3 mL/s) directly followed by 20 mL of physiologic saline solution.

Given that the multi-echo acquisition was run as part of a split-dynamic MRI framework, simulations were performed to investigate whether the splitting of dynamic time-series influences the reliability of parameter estimation in comparison with a continous acquisition. The simulations are described in Appendix A.

Image Analysis

Diagnostic radiological TNM stages were assessed according to international guidelines and the 7th edition TNM staging system.[19] Guided by T_2-weighted and diffusion-weighted images, two radiologists with 14 (A.N.) and 7 (S.H.H.) years of experience independently contoured whole-tumor volumes of interest (VOIs) by means of free-hand delineations.

Image postprocessing was performed using the nordicICE software (NordicNeuroLab, Bergen, Norway). The dynamic change in R_1, ΔR_1, was estimated using the spoiled gradient echo (SPGR) signal equation, denoted $S_{SPGR}(t)$, assuming a linear relationship between the CA concentration and change in R_1 ($1/T_1$):

$$C_t(t) = \frac{\left(1/T_1(t)\right) - 1/T_{1,0}}{r_1} \quad (1)$$

where r_1 is the longitudinal relaxivity of the CA and $T_{1,0}$ is the T_1 of the tissue in the absent of CA. A similar linear relationship (described by r_2^*-relaxivity) was assumed for the $1/T_2^*$-dependence. Both T_1- and T_2^*-relaxivity was assumed to be equal in blood and tissue and the conversion from relaxation rate to CA concentration was, therefore, not explicitly performed (because the relaxivity term then cancels out). The signal from a SPGR sequence is given by:

$$S_{SPGR}(t) = S_0 \frac{\sin\alpha\left(1 - e^{-TR/T_1(t)}\right)}{1 - \cos\alpha\left(e^{-TR/T_1(t)}\right)} e^{-TE/T_2^*(t)} \quad (2)$$

where S_0 is proportional to the thermal equilibrium magnetization, TR is the repetition time of the sequence, TE is the echo time, and α is the flip angle. T_2^*-effects were eliminated from Eq. [2] by estimating the initial signal intensity (SI) amplitude at each time-point by least-squares fitting the multi-echo data to the assumed mono-exponential TE-dependent term:

$$S(t, TE_n) = S_{PD}(t) e^{-TE_n/T_2^*(t)} \quad (3)$$

where n=1..3, $S_{PD}(t)$ is the estimated SI in the absence of T_2^*-effects. Eq. [3] thus provided estimates of both the T_2^*-corrected signal used for $R_1(t)$ estimation as well as $R_2^*(t)$ estimation used for DSC-based analysis. Solving Eq. [2] with respect to the time-dependent R_1 gives:

$$R_1(t) = -\frac{1}{TR} ln\left(\frac{1-K(t)}{1-\cos(\alpha)K(t)}\right) \quad (4)$$

where

$$K(t) = \frac{S_{PD}(t)}{S_{PD,0}} \cdot \frac{1-E_{1,0}}{1-\cos(\alpha)E_{1,0}} \quad (5)$$

and

$$E_{1,0} = e^{-TR/T_{1,0}}. \quad (6)$$

Here, $S_{PD(t)}$ is the estimated SI in the absence of T_2^*-effects at time t, $S_{PD,0}$ is the average T_2^*-corrected SI at baseline, and $T_{1,0}$ is the pre-contrast longitudinal relaxation time. Precontrast T_1-values were estimated in six patients using a modified Look-Locker inversion recovery (MOLLI) technique. Average T_1-values ($\pm$ SD) were measured to 1528 $\pm$ 40 ms in blood and 1354 $\pm$ 103 ms in cancer tissue and used as a fixed T_1-baseline for SPGR signal conversion in arteries and tumors, respectively. The measured T_1-values in blood agreed well with literature values.[20]

The ΔR_1-time curves were then analyzed on a voxel-by-voxel basis using the extended Tofts pharmacokinetic model[7]:

$$C_t(t) = K^{trans} C_a(t) \otimes e^{-\frac{K^{trans}}{v_e}t} + v_p C_a(t) \quad (7)$$

where $\otimes$ represents the convolution operator and K^{trans} is the volume transfer constant between the plasma volume, v_p, and the extravascular extracellular space volume, v_e. An arterial input function (AIF), C_a, was obtained for each patient by extracting the ΔR_1-time curves from an artery supplying the region of interest (ROI) using an automatic cluster-algorithm,[21] and an average AIF, estimated across all patients, was generated and used for quantitative analysis. Possible voxel-wise time-delays between the AIF and tissue response were automatically corrected for using a previously published approach.[22] Voxel-wise ΔR_1-time curves were also analyzed by estimating the maximum peak enhancement ($Peak_{enh}$), time-to-peak (TTP), area under the curve (AUC), wash-in rate, and wash-out rate.

The ΔR_2^*-time curves were analyzed using the established tracer kinetic model for DSC-MRI,[23] expressing the relationship between the tissue response and the AIF, yielding semi-quantitative analysis of blood flow (BF) and blood volume (BV). Corresponding mean transit time (MTT) is given by the central volume principle: MTT = BV/BF. To minimize contamination due to CA recirculation and leakage, the dynamic ΔR_2^* data was fitted to a gamma-variate function.[24,25] For each patient, an AIF was obtained by extracting the ΔR_2^*-time curve from an artery supplying the ROI using an automatic cluster-algorithm.[21] Finally, the voxel-wise ΔR_2^*-time curves were analyzed by estimating the maximum dynamic peak change (R_2^*-$peak_{enh}$) and area under the curve (R_2^*-AUC). Due to the early onset of the first intravascular CA passage, only data from the first multi-echo segment was used for DSC-based analysis.

Statistical Analysis

Statistical analysis was performed using R version 2.10.1 (R Foundation for Statistical Computing, Vienna, Austria) and MATLAB R2015a version 8.5.0 (Mathworks, Inc., Natick, MA). The following pathological stages were grouped in the statistical analysis; T1 and T2, T3 and T4, and N1 and N2. Mann-Whitney U-test was used to evaluate associations between kinetic parameters and histopathologic data. A P-value < 0.05 was considered significant. Statistically significant parameters were further evaluated using receiver operator characteristic (ROC) curve statistics. A two-way intraclass correlation coefficient (ICC) for continuous variables was used to evaluate interobserver agreement for the measured whole-tumor VOIs.

Results

MRI Analysis

Table 2 summarizes the associations between kinetic parameters attainable with the dynamic contrast-based multi-echo sequence and histopathologic evaluation of the surgically resected specimens. Parameters showing statistically significant association with histopathology are presented as box plots in Figure 1. For patients with histologically confirmed nodal metastasis, the primary tumor showed a significantly lower K^{trans} ($P = 0.010$ for reader 1 and $P = 0.043$ for reader 2) and R_2^*-$peak_{enh}$ ($P = 0.005$ for reader 1 and $P = 0.019$ for reader 2) than patients without nodal metastasis. The corresponding area under the ROC curves (sensitivity, specificity) was 87 (71%, 90%) and 90 (86%, 90%) for reader 1, and 80 (86%, 80%) and 84 (86%, 80%) for reader 2, respectively. For reader 1, primary tumor wash-out also showed a significant association with nodal status ($P = 0.025$), corresponding to an area under the ROC curve (sensitivity, specificity) of 83 (71%, 90%). Furthermore, for reader 1, T1 and T2 tumors showed a significantly higher k_{ep} ($P = 0.045$) and BV ($P = 0.021$), compared with T3 and T4 tumors, corresponding to an area under the ROC curve (sensitivity, specificity) of 76 (78%, 75%) and 83 (71%, 90%), respectively. For reader 2, no significant associations were found between the DCE or DSC parameters and pT-stage. A mismatch between mrN and pN was found in 6 of 17 patients (35.3%), corresponding to an accuracy of 64.7%.

Figure 2 shows DCE and DSC data obtained from the multi-echo sequence in a sample case, as well as resulting parametric maps merged as an overlay on a T_2-weighted image.

Figure 3 shows data from four cases and demonstrates the added value of ΔR_2^* analysis of the primary tumor in distinguishing patients with and without nodal metastasis.

Figure 4 shows the measured AIF and VOI curves together with the corresponding gamma-variate fitted curve for a selected case. The figure demonstrates the importance of CA administration timing and acquisition length of the first multi-echo acquisition segment to include the first pass bolus.

TABLE 2. Comparison of the Functional DCE- and DSC-MRI Parameters With Histopathologic Data and Corresponding *P*-Values*

Parameters	Pathologic T-stage				*P*-Values	Pathologic N-stage		*P*-Values
	T1	T2	T3	T4	T1/T2 vs T3/T4	N-	N+	N- vs N+
A: Reader 1								
DCE-MRI analysis								
K^{trans}	0.27 ± 0.04	0.43 ± 0.02	0.30 ± 0.12	0.28	0.140	**0.37 ± 0.08**	**0.25 ± 0.09**	**0.010**
k_{ep}	**0.89 ± 0.28**	**1.20 ± 0.19**	**0.81 ± 0.22**	**0.62**	**0.045**	1.01 ± 0.25	0.76 ± 0.25	0.070
v_e	35.0 ± 9.7	37.8 ± 6.2	41.0 ± 13.5	43.6	0.190	40.0 ± 7.3	38.0 ± 14.6	0.962
v_p	1.67 ± 0.42	2.57 ± 1.41	1.74 ± 1.35	0.46	0.218	1.79 ± 1.17	1.92 ± 1.36	0.962
AUC	272 ± 76	341 ± 55	379 ± 145	358	0.411	364 ± 80	314 ± 150	0.315
$Peak_{enh}$	1.87 ± 0.51	2.44 ± 0.19	2.13 ± 0.64	1.84	0.675	2.29 ± 0.31	1.89 ± 0.70	0.193
TTP	46.4 ± 48.0	19.8 ± 4.5	77.1 ± 87.0	117.8	0.162	39.0 ± 37.5	87.1 ± 91.9	0.364
wash-in	0.09 ± 0.02	0.13 ± 0.01	0.10 ± 0.04	0.06	0.218	0.11 ± 0.02	0.09 ± 0.04	0.230
wash-out	0.0007 ± 0.0005	0.0016 ± 0.0014	0.0006 ± 0.0007	0.0002	0.116	**0.0012 ± 0.0010**	**0.0004 ± 0.0006**	**0.025**
DSC-MRI analysis								
BF	196 ± 50	257 ± 23	186 ± 71	122	0.138	226 ± 56	167 ± 61	0.088
BV	**22.3 ± 6.3**	**23.6 ± 8.1**	**14.7 ± 6.0**	**12.4**	**0.021**	20.8 ± 7.1	15.1 ± 6.9	0.109
MTT	6.21 ± 1.99	5.25 ± 1.84	4.48 ± 1.26	4.90	0.200	5.20 ± 1.59	4.95 ± 1.75	0.887
R_2^*-*AUC*	440 ± 130	614 ± 273	368 ± 158	311	0.075	509 ± 204	340 ± 150	0.088
R_2^*-$Peak_{enh}$	25.5 ± 1.9	39.3 ± 6.7	28.9 ± 10.2	15.3	0,321	**35.0 ± 8.1**	**22.3 ± 6.7**	**0.005**

TABLE 2: Continued

Parameters	Pathologic T-stage				*P*-Values	Pathologic N-stage		*P*-Values
	T1	T2	T3	T4	T1/T2 vs T3/T4	N-	N+	N- vs N+
B: Reader 2								
DCE-MRI analysis								
K^{trans}	0.24 ± 0.09	0.38 ± 0.13	0.30 ± 0.11	0.27	0.411	**0.35 ± 0.11**	**0.24 ± 0.08**	**0.043**
k_{ep}	0.72 ± 0.20	0.99 ± 0.30	0.78 ± 0.20	0.56	0.286	0.87 ± 0.26	0.70 ± 0.18	0.270
v_e	36.4 ± 8.0	39.4 ± 6.7	41.1 ± 13.6	47.0	0.367	41.3 ± 6.5	38.0 ± 14.8	0.813
v_p	1.41 ± 0.74	2.42 ± 1.37	1.71 ± 1.28	0.42	0.367	1.62 ± 1.17	1.89 ± 1.30	0.601
AUC	275 ± 103	334 ± 86	377 ± 139	378	0.411	363 ± 92	314 ± 148	0.536
$Peak_{enh}$	1.85 ± 0.62	2.33 ± 0.54	2.12 ± 0.63	1.90	0.675	2.25 ± 0.46	1.88 ± 0.69	0.270
TTP	91.2 ± 123.1	44.0 ± 64.9	77.8 ± 86.4	189.3	0.734	67.1 ± 81.2	97.3 ± 99.0	0.536
wash-in	0.06 ± 0.05	0.12 ± 0.04	0.10 ± 0.04	0.06	0.858	0.10 ± 0.03	0.08 ± 0.05	0.270
wash-out	0.0005 ± 0.0007	0.0014 ± 0.0018	0.0005 ± 0.0006	0.0001	0.189	0.0010 ± 0.0012	0.0003 ± 0.0005	0.109
DSC-MRI analysis								
BF	172 ± 75	243 ± 51	186 ± 73	122	0.423	211 ± 76	166 ± 57	0.193
BV	20.3 ± 10.4	22.6 ± 10.1	14.7 ± 6.2	12.4	0.167	19.8 ± 9.1	14.7 ± 6.7	0.230
MTT	6.57 ± 2.16	5.13 ± 1.94	4.48 ± 1.28	5.08	0.321	5.37 ± 1.85	4.87 ± 1.66	0.887
R_2^*-*AUC*	403 ± 181	602 ± 315	365 ± 161	299	0.200	495 ± 239	327 ± 142	0.070
R_2^*-$Peak_{enh}$	23.3 ± 3.6	38.5 ± 8.5	28.7 ± 10.1	14.6	0.423	**33.7 ± 9.6**	**22.0 ± 6.6**	**0.019**

T1: n = 4; T2: n = 4; T3: n = 8; T4: n = 1; N-: n = 10; N+: n = 7. *P*-Values at the univariate analysis were obtained by Mann-Whitney U-test. Parameters showing statistically significant differences are highlighted in bold. K^{trans} [min^{-1}] = volume transfer constant between blood plasma and extravascular extracellular space (EES); k_{ep} [min^{-1}] = rate constant between EES and blood plasma; v_e [%] = volume of EES per unit volume tissue; v_p [%] = volume of intravascular plasma space per unit volume tissue; AUC [none] = area under the time curve; TTP [sec] = time to maximum peak enhancement; $Peak_{enh}$ [sec^{-1}] = maximum peak enhancement of ΔR_1; wash-in [none] = gradient of initial signal enhancement until maximum peak; wash-out [none] = gradient of signal decrease after maximum peak; BF [mL blood/100 g per min] = blood flow; BV [mL blood/100 g] = blood volume; MTT [sec] = mean transit time; R_2^*-AUC [none] = area under the ΔR_2^*-time curve; R_2^*-$peak_{enh}$ [sec^{-1}] = maximum peak enhancement of ΔR_2^*.
* The table shows mean (± SD) parametric values based on whole-tumor medians extracted using VOI from reader 1 (A) and reader 2 (B).

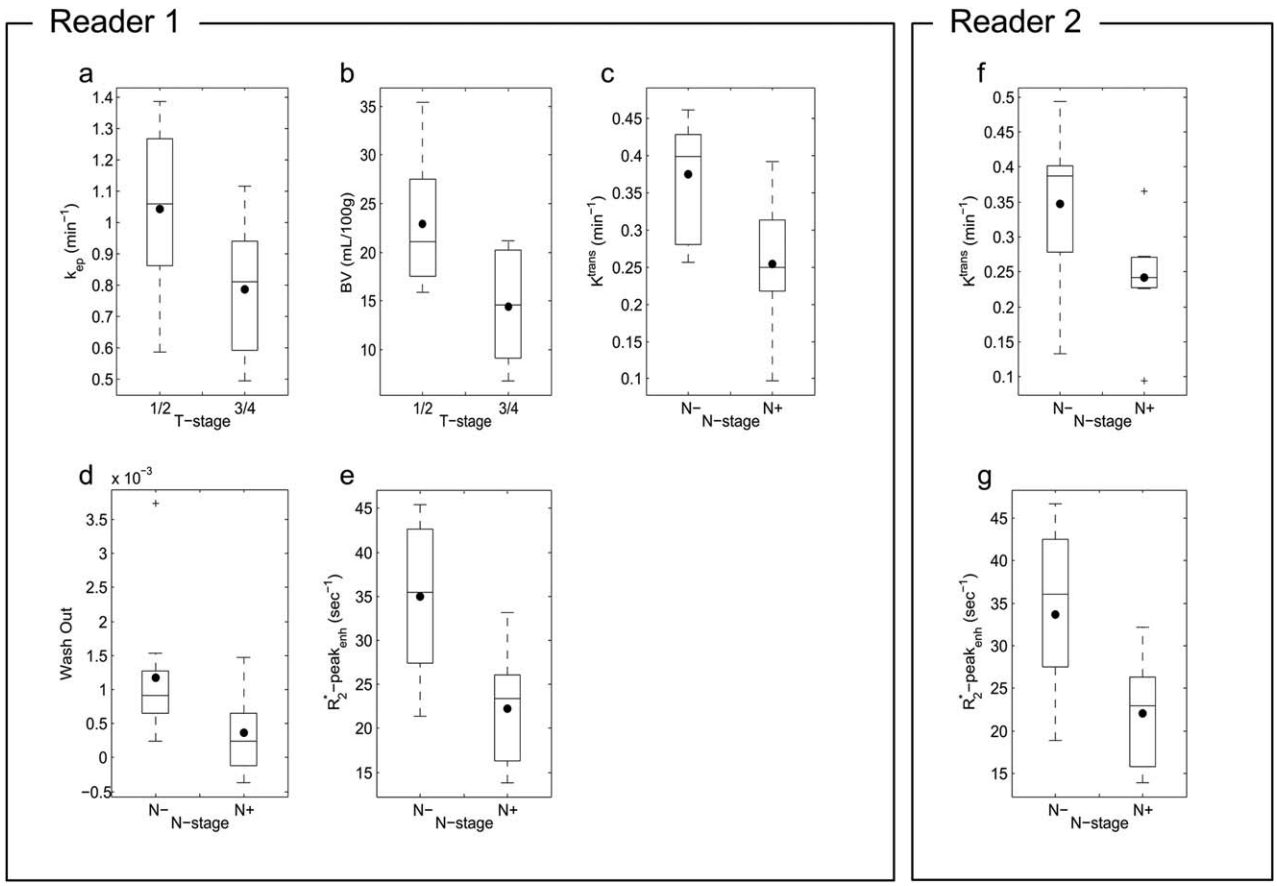

FIGURE 1: Box plots showing the parameter k_{ep} (a) and BV (b) when comparing T1- and T2- versus T3- and T4-stage tumors, and K^{trans} (c,f), wash-out (d), and R_2^*-$peak_{enh}$ (e,g) when comparing patients with and without nodal metastasis. The plotted data are based on whole-tumor medians extracted using VOI from reader 1 (a–e) and reader 2 (f,g). Box plots illustrate median (line inside box) and mean (circle inside box) values, interquartile range (box), minimal and maximal values (lines extending above and below box).

Interobserver Agreement

The ICC (95% confidence interval) between the two readers was 0.95 (0.87–0.98) for all whole-tumor VOIs, 0.81 (0.32–0.96) for T1- and T2-stage tumor VOIs, and 0.95 (0.80–0.99) for T3- and T4-stages tumor VOIs.

Simulations

Mann-Whitney U-test showed that there was no significant difference in the estimation of neither K^{trans} ($P = 0.71$), k_{ep} ($P = 0.81$), v_e ($P = 0.99$) nor v_p ($P = 0.71$) when using a continuous and a split dynamic MRI acquisition.

Discussion

Our study identified a significant association between both K^{trans} and R_2^*-$peak_{enh}$ in primary rectal tumors and the nodal status evaluated by histopathology of the surgical specimen, showing an area under the ROC curve of 87% and 90% for reader 1, and 80% and 84% for reader 2, respectively. In comparison, standard radiologic assessments of nodal status agreed with histopathologic evaluation in 64.7% (11 of 17 patients). This finding is comparable to that of a recent meta-analysis (5). Low tumor K^{trans} and R_2^*-$peak_{enh}$ were significantly associated with the presence of lymph node metastasis.

One hypothesis supporting these findings is that the peak change in tumor R_2^* reflects tissue blood supply, and that low R_2^*-$peak_{enh}$ may be associated with hypoxic tissue with insufficient blood flow. This hypothesis is supported by other results obtained in our study. First, tumor K^{trans}, which is influenced by blood flow and permeability, was also significantly lower in patients with lymph node metastasis. Second, tumor BF and $Peak_{enh}$ was lower in N+ patients compared with N- patients, consistent with reduced perfusion in a high permeability (flow limited) regime.[7] The estimated plasma volumes (v_p) were, however, similar in N- and N+ patients, which may be unexpected given the reduced flow hypothesis. There may be several reasons for the apparent lack of v_p differentiation between N+ and N- patients. First, changes in v_p and perfusion could be partially decoupled in tumors due to changes in vascular structures leading to changes in CA MTT. In a situation where perfusion is decreased but MTT is proportionally increased, v_p would remain unaffected (from the central volume principle: $BF = BV \times MTT$). Second, estimations of

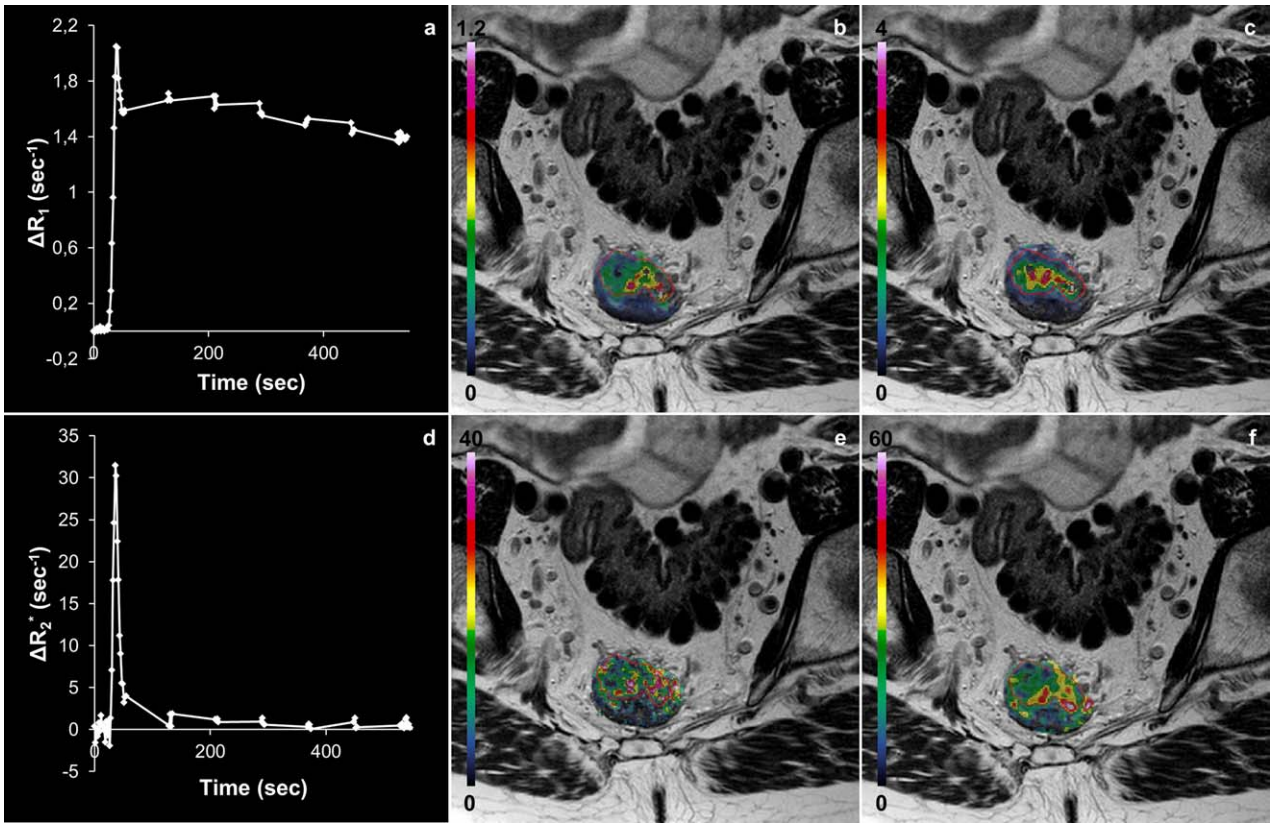

FIGURE 2: A 66-year-old male histologically diagnosed with adenocarcinoma. The figure shows high temporal resolution ΔR_1- (a) and ΔR_2^* (d) time curves. The curves were extracted using a region of interest (red outline), drawn by an experienced radiologist, delineating the tumor at a central slice. Resulting parametric maps representing K^{trans} (b), k_{ep} (c), BV (e), and R_2^*-$peak_{enh}$ (f) are shown as overlay on a T_2-weighted image.

v_p from the extended Tofts model may be unstable or insensitive to small v_p changes due to model over-fitting or water exchange effects reducing the first-pass amplitude of T_1-weighted DCE data.[26] The association between R_2^*, tumor hypoxia and blood flow is also supported by previous literature,[27,28] although their different MR data acquisition and analysis cannot be directly related to our parameter, R_2^*-$peak_{enh}$. To further investigate our hypothesis and elucidate the exact mechanism behind the associations between low R_2^*-$peak_{enh}$, low K^{trans} and lymph node metastasis, supplementary studies are required.

The nodal status represents a main prognostic marker for metastatic progression and unfavorable survival. A positive N-stage will also have implications for treatment, as these patients should be considered for neoadjuvant CRT, and extended pelvic surgery to include all lymph nodes. However, reliable staging of lymph nodes is one of the most challenging tasks in diagnostic imaging of rectal cancer. Our finding suggests that DCE- and DSC-MRI of rectal cancer may provide important indicators of lymph node status, thereby improving mrN staging prior to therapy. Similar to our findings, tumor K^{trans} values have recently been shown to be lower in N1 patients compared with N0 patients.[29] To our knowledge, associations between DSC-MRI and histopathologic data have not been reported in rectal cancer patients. However, a recent study by Goh et al showed that primary colorectal tumor blood flow measured by perfusion computed tomography (CT) was significantly lower in patients with metastatic relapse compared with disease-free patients.[30]

For one reader, our study also showed a significant association for k_{ep} when comparing T1- and T2- versus T3- and T4-stage tumors, with a lower k_{ep} being associated with higher tumor T-stage. This result is in agreement with that of a recent study showing a significantly higher mean k_{ep} in T1 stage tumors compared with T2–4 stage tumors.[29] A difference was found between the two readers when evaluating the association between histopathologic data and the DCE- and DSC-MRI derived parameters. This may be caused by a lower interobserver agreement in T1- and T2-stage tumor volumes, compared with T3- and T4-stage tumor volumes. This difference is probably caused by difficulties in delineating small tumors. The findings of a recent meta-analysis of MRI tumor staging in rectal cancer support this view. They report a lower diagnostic accuracy of staging T1 and T2 tumors compared with T3 and T4 tumors.[31]

Given that the multi-echo acquisition was run as part of a split-dynamic MRI framework, simulations were performed to investigate whether the splitting of dynamic time-

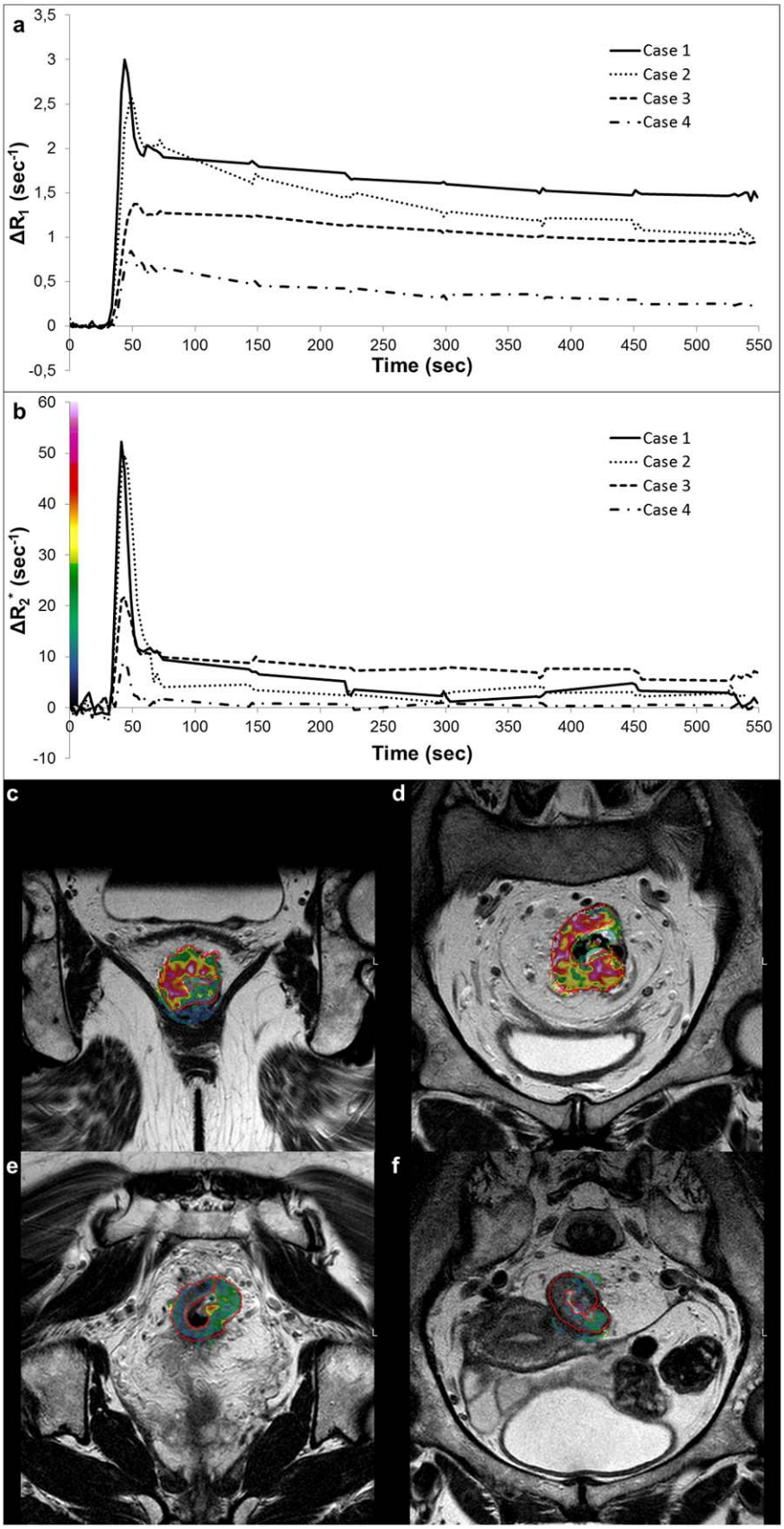

FIGURE 3: High temporal resolution ΔR_1- (a) and ΔR_2^*-time curves (b) from four rectal cancer patients, and corresponding T_2-weighted images merged with parametrical maps representing R_2^*-peak$_{enh}$ (c–f). The ΔR_1- and ΔR_2^*-time curves were extracted using a region of interest (red outline), drawn by an experienced radiologist, delineating the tumor at a central slice. Case 1 (c) and 2 (d) showed a negative pN-stage (N-), whereas case 3 (e) and 4 (f) showed a positive pN-stage (N+). Note the difference in ΔR_2^*-time curves where the N- tumors showed a strong transient increase during the bolus first-pass while the N+ tumors showed lower R_2^*-enhancement. This can also be seen in the parametric maps where the N+ tumors showed an overall low dynamic change in R_2^*, whereas the N- tumors appear highly heterogeneous with hot-spots demonstrating a strong increase in R_2^*.

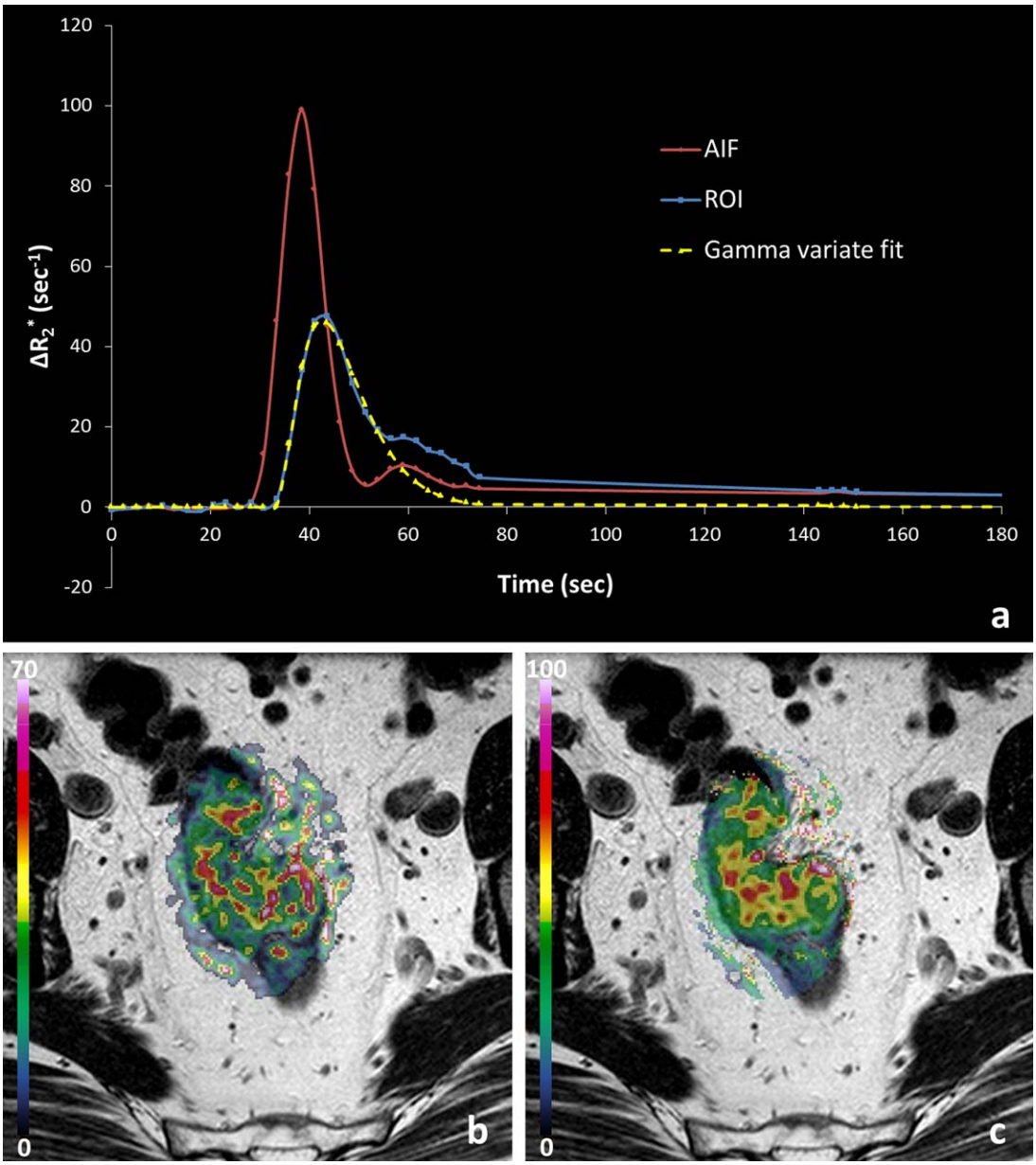

FIGURE 4: A 67-year-old male histologically diagnosed with adenocarcinoma. The figure shows the AIF automatically detected together with the average ΔR_2^*-time curves during bolus first pass (a). The corresponding gamma-variate-fitted curve is shown as dotted line. The average ΔR_2^*-time curves were extracted from a central slice. Parametric maps representing BV (b) and R_2^*-peak$_{enh}$ (c) are shown as overlay on T_2-weighted image.

series may influence the reliability of parameter estimation in comparison with a continous acquisition. According to our simulations, the split dynamic acquisition did not significantly affect the accuracy of kinetic parameter estimates compared with using a continuous acquisition. Uncertainties in the estimates were found to increase with increasing parametric value for both acquisition methods, with a somewhat larger error for the split dynamic approach. This may indicate that the splitting process reduces the sensitivity to accurately estimate extremely abnormal kinetic values. However, this difference was not statistically significant, and the findings suggest that essential information is not lost in the splitting process, and that a split dynamic approach will provide sufficient information of the contrast enhancement kinetics for clinically relevant parametric values.

Given the high vascular permeability in rectal cancer, the measured DSC data are likely contaminated by leakage effects that cannot be reliably removed by standard leakage correction approach (gamma variate fitting).[25] In theory, first-pass ΔR_2^* values could be strongly attenuated in the presence of CA extravasation due to loss of CA compartmentalization and consequent reduction in effective r_2^*-relaxivity. Leakage corrections based on kinetic modelling are successfully applied to brain DSC-MRI,[32] but these methods require access to reference data from a region with no CA extravasation and, hence, not applicable in noncentral

nervous system applications. Alternative correction methods have been proposed in the brain, where the tissue residue function is corrected directly.[33] These more advance approaches were not tested in the current study due to limited signal-to-noise ratio (SNR) and additional modelling complexity due to variable temporal resolution. It should be noted that leakage effects alone are unlikely to explain the reduced R_2^*-peak$_{enh}$ in N+ patients compared with N- patients. Because N+ subjects also had lower K^{trans}, it would be expected that leakage effects were less dominant in these patients and hence R_2^*-peak$_{enh}$ less under-estimated compared with the N- cases. Correction for CA leakage effects should, therefore, potentially lead to an even greater differentiation in perfusion metrics between the N+ and N- patients.

R_2^* peak$_{enh}$ can be considered a pseudo-marker for tissue perfusion in the limiting case when the AIF can be approximated by a delta function. In practice, CA dispersion requires deconvolution of the AIF from the tissue response to derive semi-quantitative estimates of perfusion (BF).[23] Deconvolution-based perfusion (BF) estimates (and corresponding estimated of BV and MTT) were additionally obtained in the present work. With the exception of BV, which was significantly lower T3/T4- compared with T1/T2-stage tumors, these parameters did not show any statistically significant association with histopathological confirmed T- or N-stages. Presence of significant leakage effects is clearly a confounding factor in this analysis, but it may still be surprising that BF was less sensitive than R_2^* peak$_{enh}$ because the two metrics should be equally affected by leakage effects. Furthermore, BF should in theory be less dependent on patient-specific variations in CA injection profiles, cardiac output, and other confounding factors. The apparent lack of sensitivity of BF in predicting T- or N-stage could be partly due to inaccurate AIF determination, and the fact that AIF deconvolution is sensitive to noise and insufficient SNR in the DSC data could thus result in low accuracy in the resulting BF estimates.[34]

Due to a relatively long TE, the first echo may be significantly affected by T_2^* signal attenuation, especially for high CA concentrations in blood, which in turn results in errors in the DCE-derived parameters. Given the multi-echo acquisition, T_2^* signal attenuation in the DCE data was corrected for by extrapolation back to TE = 0, yielding the initial SI amplitude in the absence of T_2^*-effects. This approach has recently been shown to reduce errors in DCE-derived parameters.[35]

While this study suggests that DCE- and DSC-MRI data acquired by a multi-echo sequence may aid the diagnostics of N-status in rectal cancer patients, several potential study limitations needs to be addressed. First, the results must be interpreted in light of the limited sample size of this single center study. Further studies will be performed to test our findings and evaluate the robustness and clinical utility in a larger patient cohort. Second, motion artifacts due to peristalsis represent a problem when acquiring dynamic data. To reduce motion artifacts by peristalsis, glucagon and Buscopan® were routinely administered immediately before the patient was centered in the scanner.

In this work, 5 of 24 patients were excluded due to motion artifacts, and motion correction strategies should be implemented when acquiring dynamic data from the rectum. Next, susceptibility effects and consequent T_2^*-induced signal loss due to air cavities may be a problem in this anatomical region. Furthermore, as the CA gradually accumulates in the bladder, susceptibility artifacts may occur in the late postcontrast phase, affecting the ΔR_2^* measurements in the surrounding tissue. However, due to the early onset of the first intravascular CA passage, early postcontrast data may be sufficient for the DSC analysis. Finally, due to limited spatial resolution in the multi-echo sequence, the measured SI in each voxel may be affected by partial volume effects. This can particularly be a problem when measuring an AIF from smaller arteries supplying the tissue of interest.

In conclusion, a dynamic contrast-based multi-echo MRI technique has been implemented and tested in rectal cancer patients. A significant association was found between both primary tumor K^{trans} and R_2^*-peak$_{enh}$ and nodal status, suggesting that a combined DCE- and DSC-MRI acquisition may help to determine N-status in diagnostic rectal cancer staging and, hence, enable improved patient stratification to multimodal treatment.

Acknowledgments

Contract grant sponsor: the South-Eastern Norway Regional Health Authority; contract grant number: 2012002; 2014012; Contract grant sponsor: Akershus University Hospital; contract grant number: 2639070; 2649029; 265904; Contract grant sponsor: The Olav Raagholt and Gerd Meidel Raagholt Research Foundation; Contract grant sponsor: The Norwegian Cancer Society; contract grant number: 780335

Appendix A

Simulations

A series of Monte Carlo simulations were performed to investigate whether a split dynamic acquisition technique influences the reliability of parameter estimation in dynamic MR-measurements in comparison with a conventional continous acquisition. The simulations were performed using in-house algorithm developed in MATLAB (The MathWork Inc. version 7.14.0.739 (R2012a), Natick, MA), according to a framework detailed by in a recent study.[14]

A system input function was simulated as a gamma variate function[36] with an additional exponential term to simulate steady state effects.[33] Corresponding tissue CA-concentration time curves were simulated according to the extended Tofts model[7] by randomly selecting the kinetic parameters within a defined range of values; *0.13–3.17 min^{-1}* for K^{trans}, *0–80%* for v_e and *0–20%* for v_p. The selected K^{trans}- and v_e-range were based on values previously observed in a clinical rectal cancer study,[37] and was defined as the mean value ± two standard deviations (SD). The bolus-arrival-time was randomly selected between 0 and 10 s, and a random Gaussian noise corresponding to a signal-to-noise ratio (SNR) of 20 at a temporal resolution of 2 s was added to the CA-concentration time curves. The selected SNR was based on values observed in the patient data.

To investigate the relaibility of the split dynamic acquisition technique in comparison with a conventional continous acquisition, one thousand simulations were performed with a fixed temporal resolution of 2 s. The system input function and tissue response curves were then resampled using the split dynamic scheme as implemented in the split dynamic technique, before adding noise based on the selected SNR. Kinetic parameter estimates for the continous- and splitted CA concentration time curves were then obtained.

Statistical Analysis

The goodness of fit for a given parameter estimation was evaluated by plotting the nominal parameter value against the estimated value and performing linear regression analysis, including model residuals and residual norms to the resulting plots. Mann-Whitney U-test was used to test the difference between the split dynamic acquisition and the continuous acquisition, with the null hypothesis that the data obtained from the two acquisition methods are samples from continuous distributions with equal medians. A statistical significance level of 5% was used.

References

1. Glimelius B, Tiret E, Cervantes A, Arnold D. Rectal cancer: ESMO Clinical Practice Guidelines for diagnosis, treatment and follow-up. Ann Oncol 2013;24:vi81–vi88.
2. Valentini V, Beets-Tan R, Borras JM, et al. Evidence and research in rectal cancer. Radiother Oncol 2008;87:449–474.
3. Smith JJ, Garcia-Aguilar J. Advances and challenges in treatment of locally advanced rectal cancer. J Clin Oncol 2015;33:1797–1808.
4. Ferlay J, Steliarova-Foucher E, Lortet-Tieulent J, et al. Cancer incidence and mortality patterns in Europe: estimates for 40 countries in 2012. Eur J Cancer 2013;49:1374–1403.
5. Al-Sukhni E, Milot L, Fruitman M, et al. Diagnostic accuracy of MRI for assessment of T category, lymph node metastases, and circumferential resection margin involvement in patients with rectal cancer: a systematic review and meta-analysis. Ann Surg Oncol 2012;19:2212–2223.
6. Prezzi D, Goh V. Rectal cancer magnetic resonance imaging: imaging beyond morphology. Clin Oncol 2016;28:83–92.
7. Tofts PS, Brix G, Buckley DL, et al. Estimating kinetic parameters from dynamic contrast-enhanced T1-weighted MRI of a diffusable tracer: standardized quantities and symbols. J Magn Reson Imaging 1999;10:223–232.
8. Alberda WJ, Dassen HPN, Dwarkasing RS, et al. Prediction of tumor stage and lymph node involvement with dynamic contrast-enhanced MRI after chemoradiotherapy for locally advanced rectal cancer. Int J Colorectal Dis 2013;28:573–580.
9. Shiroishi MS, Castellazzi G, Boxerman JL, et al. Principles of T2 *-weighted dynamic susceptibility contrast MRI technique in brain tumor imaging. J Magn Reson Imaging 2015;41:296–313.
10. Wardlaw GM, Wong R, Boylan C, Rebello R, Noseworthy MD. Investigation of a logistic model for T2* dynamic susceptibility contrast magnetic resonance imaging (dscMRI) perfusion studies. J Comput Assist Tomogr 2011;35:728–733.
11. Kvistad KA, Lundgren S, Fjøsne HE, Smenes E, Smethurst HB, Haraldseth O. Differentiating benign and malignant breast lesions with T2*-weighted first pass perfusion imaging. Acta Radiol 1999;40:45–51.
12. Kuhl CK, Bieling H, Gieseke J, et al. Breast neoplasms: T2* susceptibility-contrast, first-pass perfusion MR imaging. Radiology 1997;202:87–95.
13. Kuhl CK, Klaschik S, Mielcarek P, Gieseke J, Wardelmann E, Schild HH. Do T2-weighted pulse sequences help with the differential diagnosis of enhancing lesions in dynamic breast MRI? J Magn Reson Imaging 1999;9:187–196.
14. Grøvik E, Bjørnerud A, Storås TH, Gjesdal KI. Split dynamic MRI: Single bolus high spatial-temporal resolution and multi contrast evaluation of breast lesions. J Magn Reson Imaging 2014;39:673–682.
15. Grøvik E, Bjørnerud A, Kurz KD, et al. Single bolus split dynamic MRI: Is the combination of high spatial and dual-echo high temporal resolution interleaved sequences useful in the differential diagnosis of breast masses? J Magn Reson Imaging 2015;42:180–187.
16. Barbier E, den Boer J, Peters A, Rozeboom A, Sau J, Bonmartin A. A model of the dual effect of gadopentetate dimeglumine on dynamic brain MR images. J Magn Reson Imaging 1999;10:242–253.
17. Vonken EJPA, Van Osch MJP, Bakker CJG, Viergever MA. Simultaneous quantitative cerebral perfusion and Gd-DTPA extravasation measurement with dual-echo dynamic susceptibility contrast MRI. Magn Reson Med 2000;43:820–827.
18. Quarles CC, Gore JC, Xu L, Yankeelov TE. Comparison of dual-echo DSC-MRI- and DCE-MRI-derived contrast agent kinetic parameters. Magn Reson Imaging 2012;30:944–953.
19. Edge SB, Compton CC. The American Joint Committee on Cancer: the 7th edition of the AJCC cancer staging manual and the future of TNM. Ann Surg Oncol 2010;17:1471–1474.
20. Zhang X, Petersen ET, Ghariq E, et al. In vivo blood T1 measurements at 1.5 T, 3 T, and 7 T. Magn Reson Med 2013;70:1082–1086.
21. Murase K, Kikuchi K, Miki H, Shimizu T, Ikezoe J. Determination of arterial input function using fuzzy clustering for quantification of cerebral blood flow with dynamic susceptibility contrast-enhanced MR imaging. J Magn Reson Imaging 2001;13:797–806.
22. Singh A, Rathore RKS, Haris M, Verma SK, Husain N, Gupta RK. Improved bolus arrival time and arterial input function estimation for tracer kinetic analysis in DCE-MRI. J Magn Reson Imaging 2009;29:166–176.
23. Østergaard L, Weisskoff R, Chesler D, Gyldensted C, Rosen BR. High resolution measurement of cerebral blood flow using intravascular tracer bolus passages. Part I: Mathematical approach and statistical analysis. Magn Reson Med 1996;36:715–725.
24. Chan AA, Nelson SJ. Simplified gamma-variate fitting of perfusion curves. 2nd IEEE International Symposium on Biomed Imaging: Nano to Macro. 2004;2:1067–1070.

25. Paulson ES, Schmainda KM. Comparison of dynamic susceptibility-weighted contrast-enhanced MR methods: recommendations for measuring relative cerebral blood volume in brain tumors. Radiology 2008;249:601–613.

26. Sourbron SP, Buckley DL. On the scope and interpretation of the Tofts models for DCE-MRI. Magn Reson Med 2011;66:735–745.

27. Hoskin PJ, Carnell DM, Taylor NJ, et al. Hypoxia in prostate cancer: correlation of BOLD-MRI with pimonidazole immunohistochemistry-initial observations. Int J Radiat Oncol Biol Phys 2007;68:1065–1071.

28. Chopra S, Foltz WD, Milosevic MF, et al. Comparing oxygen-sensitive MRI (BOLD R2*) with oxygen electrode measurements: a pilot study in men with prostate cancer. Int J Radiat Biol 2009;85:805–813.

29. Yeo DM, Oh SN, Jung CK, et al. Correlation of dynamic contrast-enhanced MRI perfusion parameters with angiogenesis and biologic aggressiveness of rectal cancer: Preliminary results. J Magn Reson Imaging 2015;41:474–480.

30. Goh V, Halligan S, Wellsted DM, Bartram CI. Can perfusion CT assessment of primary colorectal adenocarcinoma blood flow at staging predict for subsequent metastatic disease. A pilot study. Eur Radiol 2009;19:79–89.

31. Zhang G, Cai Y, Xu G. Diagnostic Accuracy of MRI for assessment of T category and circumferential resection margin involvement in patients with rectal cancer: a meta-analysis. Dis Colon Rectum 2016; 59:789–799.

32. Boxerman JL, Schmainda KM, Weisskoff RM. Relative cerebral blood volume maps corrected for contrast agent extravasation significantly correlate with glioma tumor grade, whereas uncorrected maps do not. AJNR Am J Neuroradiol 2006;27:859–867.

33. Bjornerud A, Sorensen AG, Mouridsen K, Emblem KE. T1- and T2*-dominant extravasation correction in DSC-MRI: part I--theoretical considerations and implications for assessment of tumor hemodynamic properties. J Cereb Blood Flow Metab 2011;31:2041–2053.

34. Calamante F. Arterial input function in perfusion MRI: a comprehensive review. Prog Nucl Magn Reson Spectrosc 2013;74:1–32.

35. Kleppestø M, Larsson C, Groote I, et al. T_2^*-correction in dynamic contrast-enhanced MRI from double-echo acquisitions. J Magn Reson Imaging 2014;39:1314–1319.

36. Benner T, Heiland S, Erb G, Forsting M, Sartor K. Accuracy of gamma-variate fits to concentration-time curves from dynamic susceptibility-contrast enhanced MRI: influence of time resolution, maximal signal drop and signal-to-noise. Magn Reson Imaging 1997;15:307–317.

37. Lim JS, Kim D, Baek S-E, et al. Perfusion MRI for the prediction of treatment response after preoperative chemoradiotherapy in locally advanced rectal cancer. Eur Radiol 2012;22:1693–1700.